Compressive characteristics of bimodal aluminium matrix syntactic foams

Imre Norbert ORBULOV[a,b]*, Alexandra KEMÉNY[a,b], Ádám FILEP[c], Zoltán GÁCSI[c]

[a]Department of Materials Science and Engineering, Faculty of Mechanical Engineering, Budapest University of Technology and Economics, Műegyetem rakpart 3., Budapest, Hungary, 1111

[b]MTA–BME Lendület Composite Metal Foams Research Group, Műegyetem rakpart 3., Budapest, Hungary, 1111

[c]Institute of Physical Metallurgy, Metal Forming and Nanotechnology, Faculty of Materials Science and Engineering, University of Miskolc, Egyetemváros, Miskolc, Hungary, 3515

*Corresponding author

Address: Department of Materials Science and Engineering, Faculty of Mechanical Engineering, Budapest University of Technology and Economics, Műegyetem rakpart 3., Budapest, Hungary, 1111

Tel: +36 1 463 2386

Fax: +36 1 463 1366

E-mail: orbulov@eik.bme.hu

Abstract

High performance metal matrix syntactic foams (MMSFs) have been produced by liquid state infiltration of AlSi12 alloy into two loosely packed sets of different nominal diameter (150 μm and 1500 μm) oxide hollow spheres (CHSs) and their mixed packs. The structure of the MMSFs has been studied by X-ray computer tomography and microscopy. The mechanical properties were mapped by compressive tests. The structural investigations showed proper infiltration. In the case of pure small and large CHS filler, the compressive tests revealed high strength levels all over the deformation of the materials up to 50% compressive strain, with the dominance (higher strength values) of the smaller CHSs filled MMSFs. In the case of bimodal CHS filling, the compressive features of the MMSFs have been mixed with two local peaks corresponding to the failure of the smaller and larger CHS filled MMSFs. Rule of mixtures is applicable to estimate the compressive strength.

Keywords

A. Foams; B. Mechanical properties; B. Fracture; D. Mechanical testing

1. Introduction

Metal matrix syntactic foams (MMSFs), often referred as composite metal foams (CMFs) are porous materials in which a porous phase is applied as filler material to ensure porosity and therefore foam structure. In this way MMSFs also satisfy the criteria of particle reinforced metal matrix composites, since the hollow spheres can be considered as particles and there is an interface layer (adhesive and cohesive in nature) between the matrix and the hollow spheres.

Since the original aim of the production of MMSFs was to provide low-weight structural materials with high energy absorbing capacity, the matrix materials of MMSFs are often come from the light-weight alloys such as aluminium (most often, [1–12]) and magnesium [13–16]. However, efforts have been invested into the production of different MMSFs with iron- [17–19], titanium- [20–22] or zinc [23–28] alloys. Regarding the filler of MMSFs the first studies have been done on fly-ash cenospheres [29–32] as hollow mixed oxide, porous and cheap by-product of thermal power plants, with large scatter in the properties of the individual particles. In order to control the scatter in the mechanical properties of the MMSFs, the investigations turned to the more precise hollow spheres including pure alumina [33–36], silicon carbide [37,38] or some kind of metal, mainly steels [39–41]. Later, alternative filler materials such as expanded perlite [42–49] or pumice [50] have been investigated in order to decrease the costs of the MMSFs.

The above mentioned studies have been dealt with MMSFs in which only one kind of filler was applied to produce the porous structure. However, the possibility of the application of mixed fillers is more or less evident. Rare examples for this approach can be found in the literature. For example, hybrid MMSFs have been produced by the combination of ceramic and metallic hollow spheres (CHSs and MHSs, respectively) [51–54]. In these publications the feasibility of infiltration as production method, the tribological, the microstructural and the mechanical properties have been studied. Regarding the production, the pressure infiltration was found to be a convenient method to produce hybrid MMSFs with mixed ceramic and metallic hollow sphere content (with different ceramic and metallic filler ratios). According to the microstructural investigations scanning electron microscopy (SEM) and energy dispersive X-ray spectrometry (EDS) along lines perpendicular to the interface region between the hollow spheres and the matrix material revealed a cohesive connection between

the constituents with an interface layer thickness less than 10 µm. In the case of metallic (Fe based) hollow spheres Fe was dissolved into the AlSi12 matrix, while in the case of ceramic (mixture of Al_2O_3 and SiO_2) hollow spheres an exchange reaction happened between the SiO_2 content of the CHSs and the Al content of the AlSi12 matrix, that was hindered by the relatively high Si content of the matrix. Regarding the compressive properties, the yield strength at 1% engineering compressive strain, the compressive strength and the plateau strength increased, while the fracture strain decreased by the increment of the CHSs in the filler mixture. The relationship between the compressive and plateau strength and the amount of CHSs was found to be linear. In this way, the mechanical properties of the produced MMSFs can be set and tailored to the values required by the given application. Beside the strength values, the failure mode of the MMSFs have been also changed between plastic collapse and brittle shearing by the increment of CHSs ratio. Since the amount of CHSs influenced the strength and fracture behaviour as well, the absorbed mechanical energy showed a local minimum at ~60% MHS and ~40% CHS content. Compared to this local minimum, in the case of higher CHS content the strength values were higher and in the case of higher MHS content the ductility of the MMSFs balanced the lower strength values and therefore, the MMSFs absorbed more mechanical energies in both cases.

In their brief study, Tao et al. [55] investigated the application of two different size CHS grades to increase the energy absorption capability of the produced MMSFs. The applied matrix material was a 6082 grade Mg-Si alloyed aluminium, while the CHSs consisted of ~40% Al_2O_3 and ~60% SiO_2, with the size ranges of 75-125 µm (fine) and 250-500 µm (coarse) with an effective density of 0.6 gcm^{-3}. By the mixing of the fine and coarse particles, the authors managed to decrease the overall density of the MMSFs by 25% (ensuring 10% higher porosity). The MMSFs with mixed CHSs showed an almost horizontal, flat and relatively high (~60 MPa) plateau regime beside good ductility (~40% compressive strain up to the start of the densification) [55].

Besides the particular example of MMSFs, the mixing of different size spherical particles is an interesting problem in general. According to this, Brouwers [56] addressed the geometric random packing and void fraction of bimodal and polydisperse particles. In the special case of bimodal particles – in which case one of the particle sets is called ‘large’ and the other is referred as ‘small’ particles – the void fraction between the particles can be determined based only on the diameter ratio of the large (d_L) and small (d_S) particle fractions. The most important finding of the paper in the viewpoint of bimodal MMSFs is that, for ‘saturated mixtures’ (if the larger particles can be considered infinitely larger than the smaller ones ($d_L/d_S \rightarrow \infty$ in theory and $d_L/d_S > 7 \ldots 10$ in practice) in which the two groups of particles are noninteracting, the lowest void fraction can be obtained when the volume fraction of large and small particles tends to 2/3 and 1/3, respectively [56].

The main aims of this paper are (i) to successfully produce high porosity, low void fraction, high performance, bimodal MMSFs and (ii) to investigate and report their microstructural features and mechanical properties in comparison to the MMSFs produced with pure small and pure large CHSs.

2. Materials and Methods

AlSi12 aluminium alloy was applied as matrix material to produce MMSFs by low pressure inert gas liquid state infiltration (previously detailed in [54]). The chemical composition of the matrix alloy, measured by optical emission spectrometry (WAS PMI Master Sort device) is listed in Table 1. The specific alloy was chosen due to its good castability and fluidity, that are both advantageous in the infiltration technological viewpoint.

Table 1. Chemical composition of the matrix (in wt%)

Alloy	Al	Si	Fe	Mg	Zn	Mn	Cu
AlSi12	87.019	12.830	0.127	0.010	0.007	0.005	0.002

As filler material, two grades of mixed oxide CHSs were applied. The first, larger diameter group was provided by Hollomet GmbH under the tradename 'Globocer'. Their diameter measured on numerous individual hollow spheres was found to be Ø1425 ± 42.2 µm, with a wall thickness of 60 ± 1.7 µm. The tapped bulk density of these particles was measured to be 0.816 gcm^{-3}. These spheres are designated by '(L)' in the micrographs. The second, smaller diameter group was delivered by Envirospheres pty. Ltd. under the tradename 'SL300'. The diameter of these CHSs was Ø150 ± 4.1 µm (one magnitude smaller compared to the 'Globocer' grade CHSs), with a wall thickness of 6.75 ± 0.20 µm, their average tapped bulk density was 0.691 gcm^{-3}. . These spheres are designated by '(S)' in the micrographs. The nominal wall thickness to diameter ratios in the case of larger and smaller CHSs were 0.0421 and 0.0450, respectively. These ratios can be considered identical, therefore the mechanical load bearing capacity of the CHSs are very close to each other. The chemical composition of both CHS grade was identical and contained 33 wt% Al_2O_3, 48 wt% SiO_2 and 19 wt% $3Al_2O_3 \cdot 2SiO_2$ (mullite). Three kinds of MMSF blocks were produced: (i) with pure large CHSs, (ii) with pure small CHSs and (iii) with the saturated mixture of the small and large CHSs to produce bimodal MMSFs.

The produced MMSFs were investigated on various scales, the macrostructure was mapped by X-ray computer tomography (CT) on an YXLON FF35 MicroCT equipment (microfocus X ray tube, transmission beam, 65 KV, voxel size 5.35 µm), the microstructure was investigated by light optical microscopy (LOM) on an Olympus PMG3 microscope and by scanning electron microscopy (SEM) on a Zeiss EVO MA10 microscope extended by energy dispersive X-ray spectroscopy (EDS). As the main load mode of the MMSFs is the compression, the mechanical properties of the MMSFs were measured and evaluated by standardized compressive tests [57] on Ø15 mm (D) cylindrical samples with a MTS810 universal hydraulic testing machine. The samples' height (H) were varied and different aspect ratios (H/D= 1.0, 1.5 and 2.0) were applied, resulting in heights of 15.0 mm, 22.5 mm and 30.0 mm, respectively. The cross-head speed was set to 0.1 mms^{-1} and the samples were compressed up to 50% compressive strain in engineering system. Five-five samples were tested for each configuration and their main characteristic properties, such as the compressive strength (σ_C (MPa)), fracture strain (the strain at the compressive strength, ε_C (%)), structural stiffness (S (MPa)), fracture energy (W_C (Jcm^{-3})), absorbed mechanical energy (up to 50% engineering strain, W (Jcm^{-3})) were measured.

3. Results and Discussion

3.1. Macrostructure

The macrostructure of the bimodal MMSFs has been studied by X-ray CT to reveal the arrangement of the CHSs and to gather information about the distribution of the individual CHSs [58–61]. It is important in the isotropic and constant material properties point of view to have homogeneous saturated mixture of the CHSs. The full 3D scans of the bimodal MMSFs are shown in fig. 1.

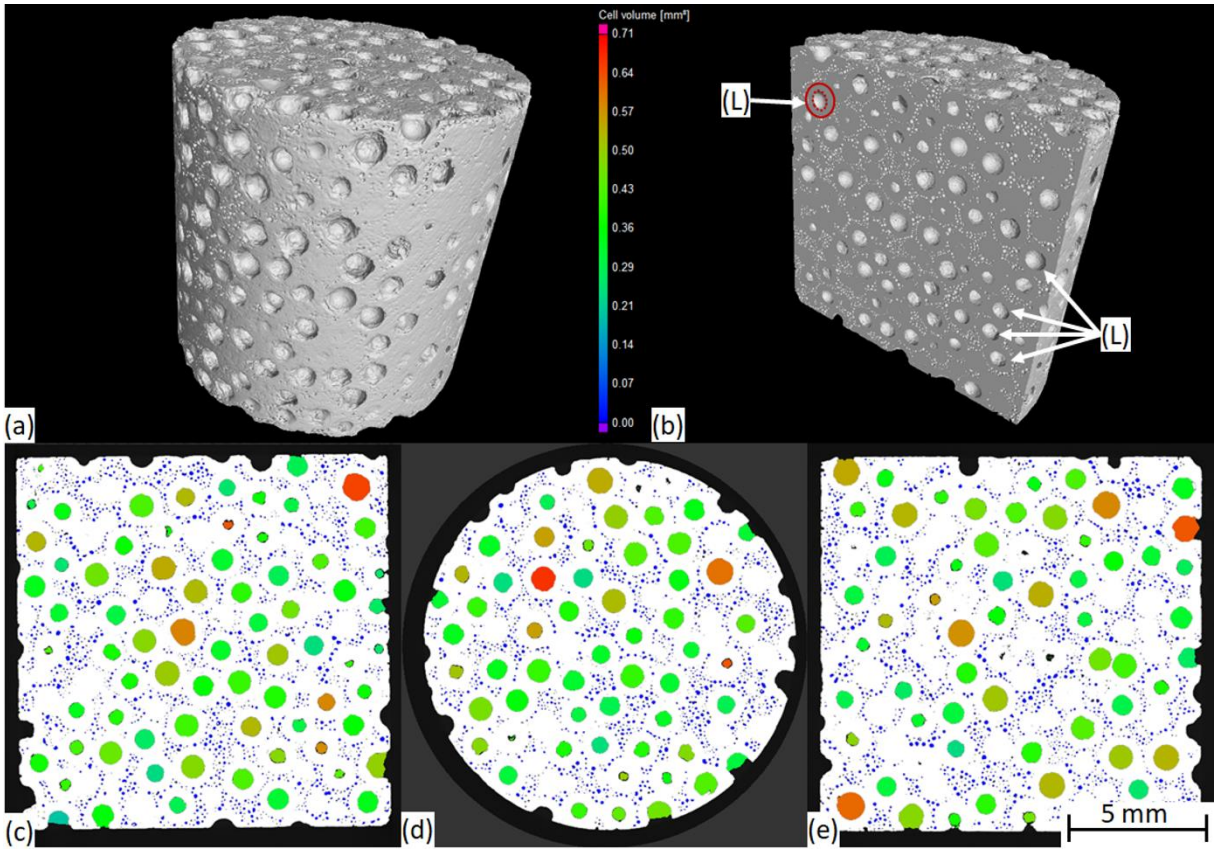

Figure 1. CT images of the produced bimodal MMSF (a) the investigated sample, (b) longitudinal 3D section, (c) front view of the sample, (d) top view of the sample and (e) side view of the sample. Images (c-e) were taken in the middle planes.

Fig. 1 proves homogeneous distribution of larger and smaller CHSs as well. The inner porosity of the larger CHS grade is running from green to purple, while the smaller ones are blue. The sections, taken in the representative middle planes of the three spatial dimensions of the sample shows even distribution of the larger CHSs, while the smaller ones are situated in the voids between the larger CHSs to form a saturated mixture. According to Brouwers [56], as the diameter ratio of the applied larger and smaller spheres is d_L/d_S = 9.5, the overall void fraction in the bimodal system is ~32.8%, in other words, 67.2% of the volume is occupied by the CHSs (designated as V_{CHS}), from which 2/3 is covered by the larger and 1/3 is covered by the smaller CHSs. Considering an individual hollow sphere with outer diameter of D and wall thickness of t, one hollow sphere can cause a porosity equal to its inner void. For an individual sphere this porosity (P_i) can be calculated as

$$P_i = \frac{V_i}{V_o} = \frac{d^3\pi/6}{D^3\pi/6} = \left(\frac{d}{D}\right)^3 = \left(\frac{D-2t}{D}\right)^3 = \left(1-\frac{2t}{D}\right)^3 \quad (1)$$

where V_i and V_o are the inner and overall volume of the hollow spheres, d and D are the inner and outer diameters of the hollow spheres and t is the wall thickness. For the larger CHSs P_L = 76.80%, while for the smaller CHSs P_S=75.36%. If the CHS occupied volume is divided according to the findings of Brouwers (2/3 larger and 1/3 smaller CHSs, respectively), the overall porosity of MMSF can be computed as

$$P = \left(\frac{2}{3}P_L + \frac{1}{3}P_S\right)V_{CHS} \quad (2)$$

The overall porosity is calculated as 51.3% as it was confirmed by the X-ray CT investigations: the measured overall porosity was found to be 1032 mm^3, while the overall volume of the sample was detected as 2093 mm^3, this leads to an overall porosity of 49.3%, that is in good agreement to the calculated porosity. On the other hand, the porosity can be calculated based on the bulk density of the CHSs' walls (ρ_{wall}) and on the tapped bulk density of the CHS set (ρ_{CHS}), according to eq. 3.:

$$P_i = V_{CHS} \frac{\rho_{wall} - \rho_{CHS}}{\rho_{CHS}} \quad (3)$$

The density of the wall material can be estimated based on the chemical composition of the CHSs and taken as 3.17 gcm^{-3}. Considering the tapped bulk densities of the larger (0.816 gcm^{-3}) and the smaller (0.695 gcm^{-3}) CHSs, the calculated porosities are 33.3% for the larger and 17.5% for the smaller CHSs, respectively. The overall porosity is the sum of the porosities ensured by the different CHSs and equals to 50.8%, that is also in good agreement with the previously (geometrical features based) calculations and with the results of the X-ray CT investigations as well.

3.2. Microstructure

The microstructure of the produced MMSFs were studied by optical microscopy. typical cross-sectional images of the produced structure are shown in fig. 2.

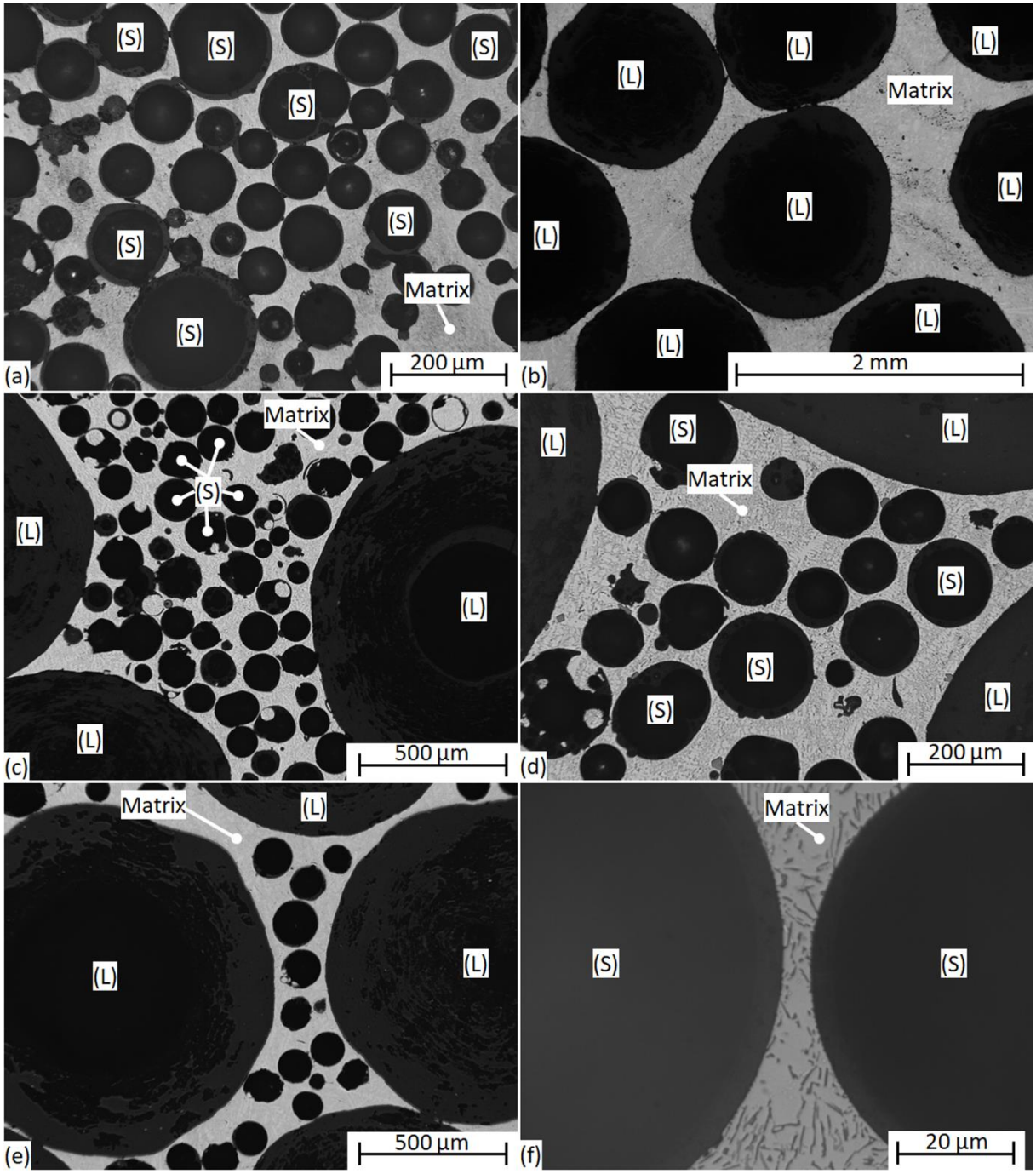

Figure 2. Representative micrographs of (a) pure small CHS filled, (b) pure large CHS filled and (c-f) bimodal MMSFs.

Fig. 2a shows the representative microscopic image of a pure small CHS filled MMSF. The infiltration can be qualified as good, the volume of unintended porosity between the CHSs is negligible and there are no infiltrated CHSs in the material. Fig. 2b represents the microstructure of pure large CHS filled MMSFs. The infiltration is satisfying in this case too and the eutectic microstructure of the AlSi12 matrix can be also observed. Fig. 2c shows an overall figure about a bimodal MMSF, the larger and the smaller CHSs can be clearly observed. In the case of bimodal MMSFs the infiltration is a more complex procedure than in the case of pure unimodal filler, in order to overcome this problem, the infiltration pressure has to be increased, that resulted in a few infiltrated smaller CHS. Fig. 2d is a

magnified image in which the eutectic microstructure of the matrix can be also observed. Fig. 2e is emphasizing the proof of the saturated mixture of the smaller and larger CHSs, while fig. 2f is the magnified image of the eutectic microstructure between two small CHSs in a bimodal MMSF. The microstructure was also investigated by SEM (fig. 3). Besides the observation of the structure, the interface layer between the CHSs and the matrix was studied.

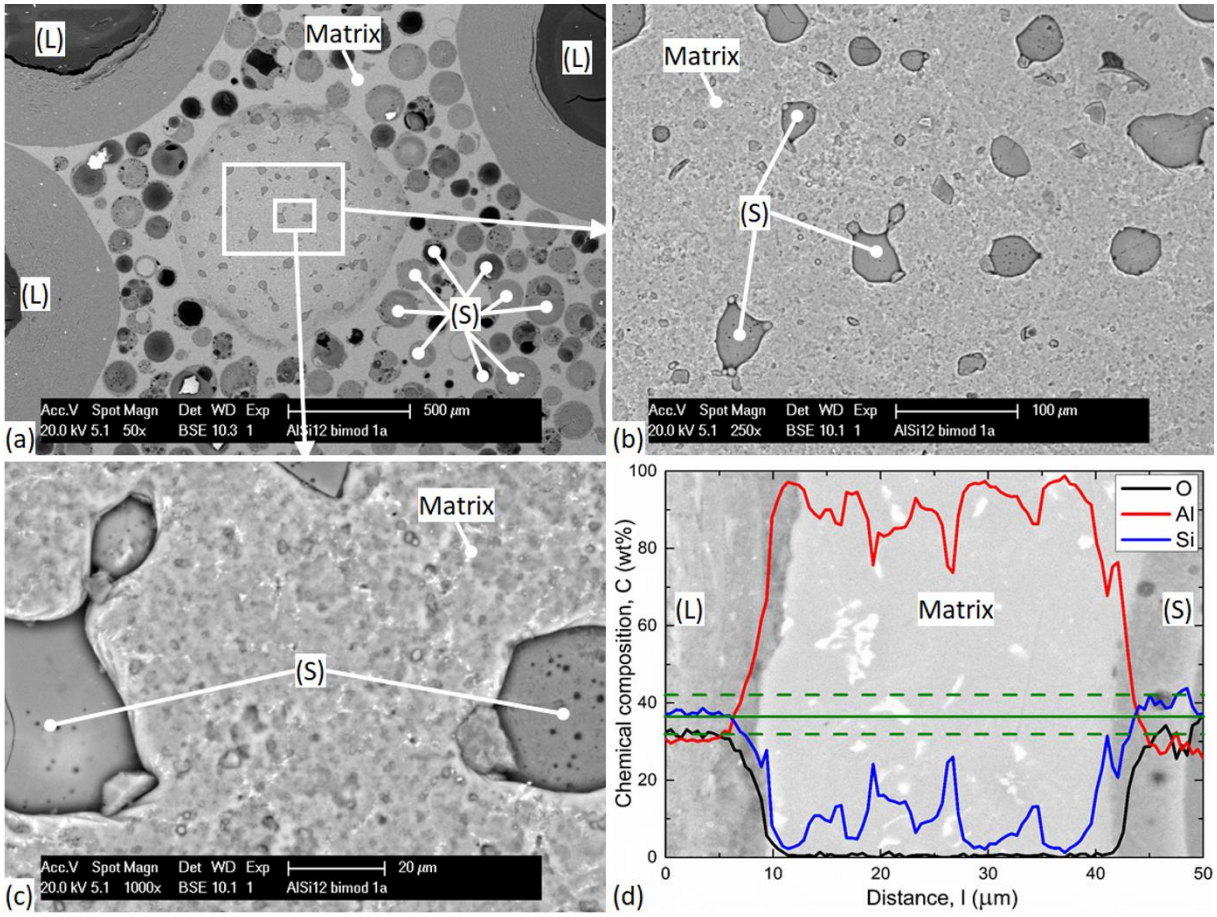

Figure 3. SEM images of MMSFs (a) general overview of the cross-section, (b-c) magnified views from the middle of (a) and (d) line EDS results.

Fig. 3a shows the representative SEM overview of the bimodal MMSFs, in the middle the place of a removed larger sphere can be observed. In fig. 3b the magnified view of the middle part can be seen, the lighter grey phase is the AlSi12 matrix and the darker grey spots are smaller CHSs below the surface, that were in connection with the removed larger CHS. In fig. 3c, the image of fig. 3b is shown in higher magnification: the solidified front of the matrix material can be clearly observed. In this particular example, the melt was unable to fully infiltrate the thin gaps between the smaller CHSs and the removed larger CHS due to the high contact (wetting) angle and wetting conditions. The bond between the CHSs and the matrix material is very important, therefore the interface layers between the small and large CHSs and the AlSi12 matrix were investigated, respectively as it is shown in fig. 3d. In the subfigure a larger and a smaller CHS (marked by (L) and (S) respectively) can be observed on the left and on the right side of the figure; in the middle – between the spheres – the matrix material (marked by (M)) can be seen. The line EDS measurement was performed along the continuous horizontal green line (additionally the estimated volume from which the measurement results were gathered is marked by dashed green lines). The chemical composition changes can be

tracked along the investigation line. The black curve is showing the O amount that can be found only in the CHSs corresponding to their mixed oxide composition (refer to section 2). The Al and Si content are changing parallel in the matrix according to the actual presence or lack of the Si lamellae in the eutectic matrix (white blocks in fig. 3d). The thickness of the interface layer can be estimated from the sudden changes of each chemical element and the found to be ~6 µm and ~9 µm in the case of larger and smaller CHSs, respectively. These thin interface layers are due to the diffusional chemical reaction between the silica and Al content of the CHSs and the matrix (driven by the Si mismatch of the constituents), suppressed by the relatively high Si content of the matrix [62].

3.3. Mechanical properties

In this section the compressive mechanical properties of the produced MMSFs are introduced according to the ISO 13314:2011 standard and with respect to the H/D ratio. The compressive strength (σ_C (MPa)), the fracture strain (the strain at the compressive strength, ε_C (%)), the structural stiffness (S (MPa)), the fracture energy (W_C (Jcm^{-3})) and the absorbed mechanical energy (up to 50% engineering strain, W (Jcm^{-3})) were tracked. The registered curves are plotted in fig. 4.

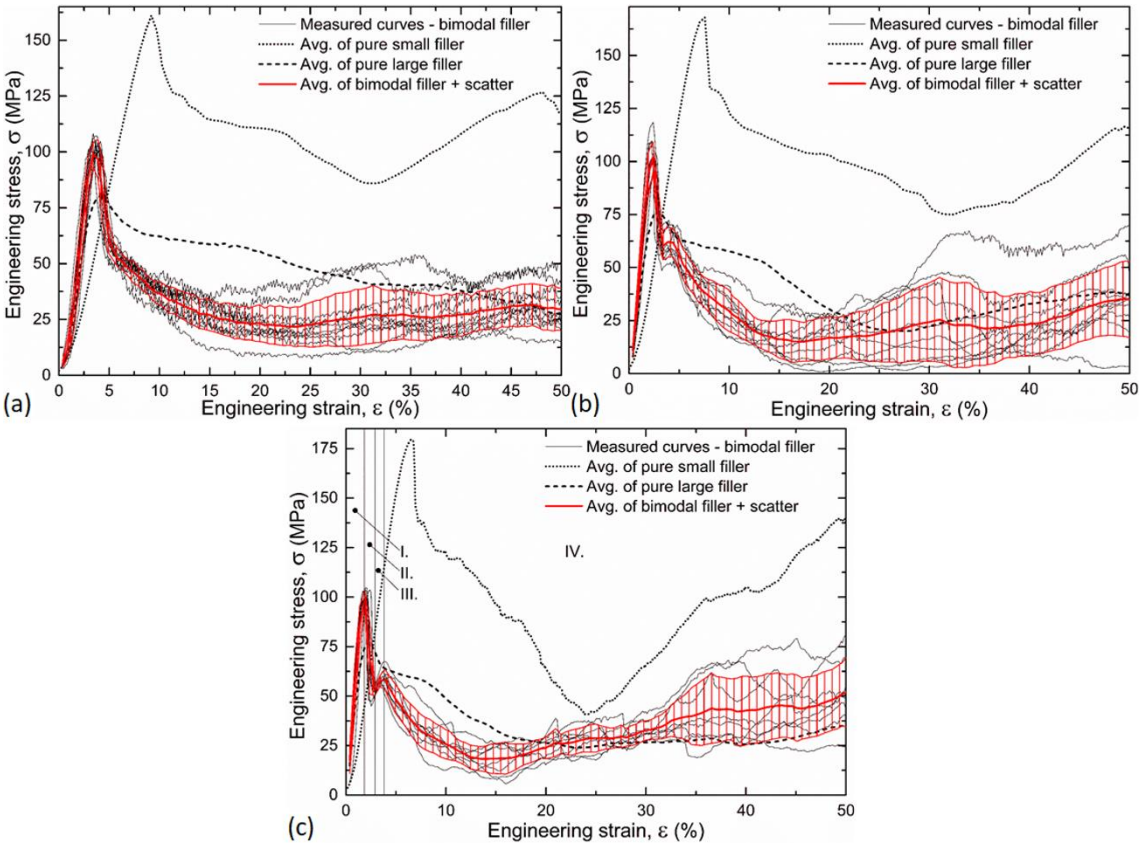

Figure 4. Engineering tress – engineering strain curves of MMSFs, with respect to their aspect ratio (a) H/D=1.0, (b) H/D=1.5 and (c) H/D=2.0

Considering the bimodal MMSFs, the engineering stress – engineering strain curves (plotted as thin black lines in fig. 4) were averaged in order to get statistical results, the averaged curve with its scatter band is plotted in red in fig. 4. The average stress – strain curve can be divided into four stages (designated by Roman numbers in fig. 4c). Along the first stage, the stress – strain relationship is linear and macroscopically the sample behaved as a linear elastic material. As it was shown in previous studies, minor plastic deformation may occur during this section [63,64]. The first stage ends up in a local peak and the coordinates of this peak are considered as the compressive strength ($\sigma_{C\text{-}I}$ (MPa)) and fracture strain ($\varepsilon_{C\text{-}I}$ (%)) of the MMSFs, respectively. The mechanical energy absorbed

up to the first peak is referred as the fracture energy (W_C (Jcm^{-3})) and can be interpreted as some kind of toughness parameter of the MMSFs [65]. The slope of the section equals to the structural modulus (S (MPa)) of the MMSFs. In the second stage a sudden stress drop appeared in the diagram, that can be connected to the appearance of the first damage zone in the sample, while due to the sudden deformation the stress level dropped. This failure type is common in the case of small CHS filler [1,66] and it was inherited to the bimodal MMSFs as well. Subsequently, a stress rise started and ended up in a second local peak at significantly lower stress level ($\sigma_{C\text{-}II}$ (MPa) at $\varepsilon_{C\text{-}II}$ (%), stage III). Please note that this feature was suppressed in the case of H/D=1, in which the sample could not accommodate an additional cleavage like failure and the whole sample deformed more or less homogeneously. This was also found by Tao et al. [55] with their H/D=1 aspect ratio samples. In the case of larger samples, a secondary cleavage crack appeared and was represented by the second peak in the stress – strain curve (see the failure modes in Section 3.4). The amplitude of this secondary crack was higher, as the aspect ratio increased. The longest stage (IV) in the diagram is referred as the plateau region and finally, the area under the whole stress – strain curve is considered as the overall absorbed mechanical energy W (Jcm^{-3}).

For better comparison, the stress – strain curves of pure small and pure large CHS filled MMSFs are plotted as dotted and dashed lines in fig. 4, respectively. The pure small CHS filled MMSFs showed extreme compressive strength values connected to considerable fracture strains and this combination results in large fracture energies. In the structural material viewpoint, these MMSFs are the best choice, obviously. However, the stress drop after the compressive strength is quite large (~30%) and the plateau region forms a large, 'V' like valley, that is not the most suitable for energy absorption purposes. On the other hand, the pure large CHS filled MMSFs had significantly smaller compressive strength, but the sudden stress drops and the valley in the plateau region are missing. These MMSFs failed due to subsequent collapse of the CHSs, instead of the rupture reported in the case of smaller CHS filler [1] (see Section 3.4). The energy absorption in the plateau region is more even, and happens at lower stress levels, resulting in lower acting forces, therefore these materials would be more ideal for collision damping rather than structural applications. The abovementioned characteristic properties of the MMSFs are plotted in fig. 5.

Further analysis of the results indicates that, the compressive strength of the bimodal structure lays between the pure small and pure large CHS filled MMSFs (fig. 5a). The compressive strength values were not influenced by the aspect ratio in any CHSs configuration. The first compressive strength can be estimated by the rule of mixtures:

$$\sigma_{C-I}^{bimodal} = V_{CHS}^{large}\sigma_{C-I}^{large} + V_{CHS}^{small}\sigma_{C-I}^{small} \quad (4)$$

where V denotes the volume fraction of the given CHSs, respectively. The calculation leads to an estimated $\sigma_{C\text{-}I}$ = 108 ± 4.3 for the bimodal MMSFs, that is in good agreement with the measured one. The fact of the applicability of the rule of mixtures ensures design options for the actual composition (ratio of the small and large CHSs) of the bimodal MMSFs in order to tailor their properties to the requirements of a given application. Compared to the literature [55], the produced bimodal MMSFs proved higher compressive strength values (~110 MPa) than the published results in [55] (~80 MPa); however, the distribution of the CHSs and the production method were similar. The main difference can be found in the matrix material (6082-T6 in [55]) and in the quality of infiltration.

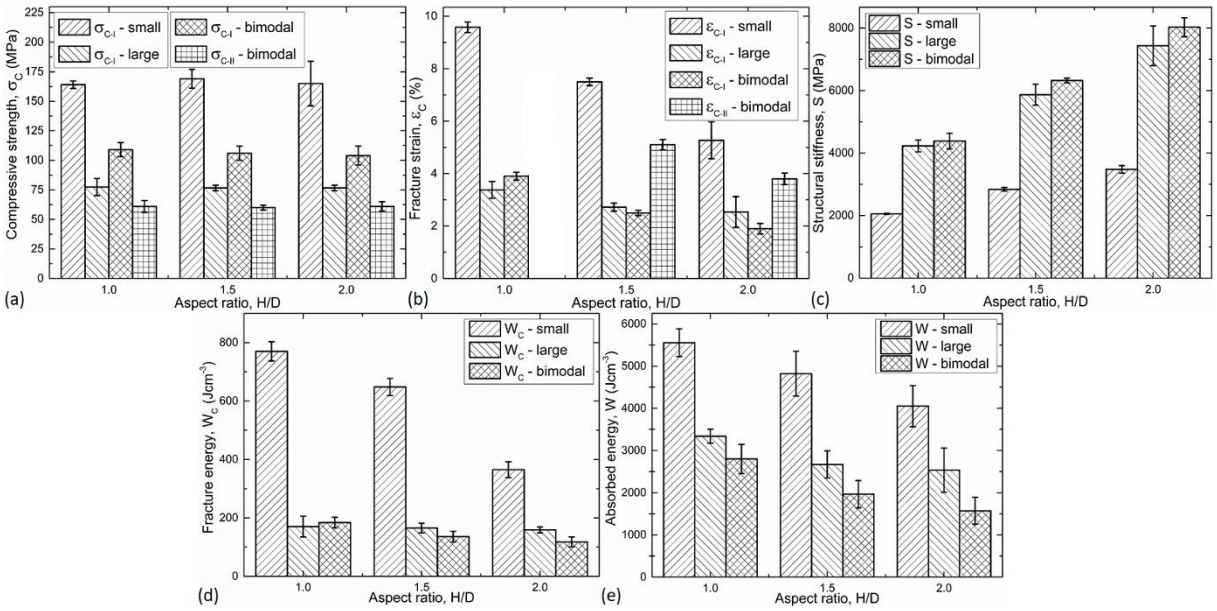

Figure 5. Mechanical properties of MMSFs (a) compressive strength, (b) fracture strain, (c) structural stiffness, (d) fracture energy and (e) absorbed energy

Regarding the fracture strains (fig. 5b), the pure small CHSs ensured the largest fracture strains, followed by the pure large CHS and the bimodal structures. The reason behind this is in the complex relationship of the compressive strength and the structural stiffness (fig. 5c), that changes reversely: the highest stiffness was shown by the bimodal MMSFs, followed by the pure large and pure small CHS filler, respectively. The slightly higher structural stiffness of the bimodal structure can be attributed to the phenomenon presented in the first three subfigures of fig. 3 as the smaller CHSs are in touch with the larger ones in numerous points and therefore can ensure a better support for the larger ones with thicker walls resulting in a higher stiffness because of the numerous ceramic contact points. Considering the scatters of the structural stiffness, this property was dominated by the features of the larger CHSs. The fracture energies (fig. 5d) are determined by the compressive strength values and the by fracture strains. The fracture strains were again dominated by the large CHSs due to their lower compressive strength values. The whole absorbed energy (fig. 5e) was the highest in the case of small CHS, but the way of the energy absorption has to be noted uneven, therefore this type is not recommended as collision dampers for instance. The other two grade of MMSFs represented more or less even energy absorption, the lowest stress level belonged to the bimodal structures. This could be advantageous in the case of collision damping requiring 'soft' transmission of the reaction forces. Higher energy absorption levels could be ensured by longer damping routes and / or by constrained deformation of the MMSFs [67].

3.4. Failure modes

In the case of bimodal MMSFs two different failure modes were distinguished with respect to the actual aspect ratio (H/D) of the samples. The failure modes are depicted in figs. 6 and 7, respectively. Regarding the H/D=1 case, the appearance of the first damage zone is connected to the collapse of the weakest hollow spheres in a distinguished layer, usually near to the middle of the sample (fig. 6a). This phenomenon can be identified as a stress drop in the stress – strain curves after a moderately sharp peak stress level (fig. 4a). As the deformation proceeded, this damaged layer was thickened (fig. 6b) and finally the whole sample collapsed (fig. 6c and 6e).

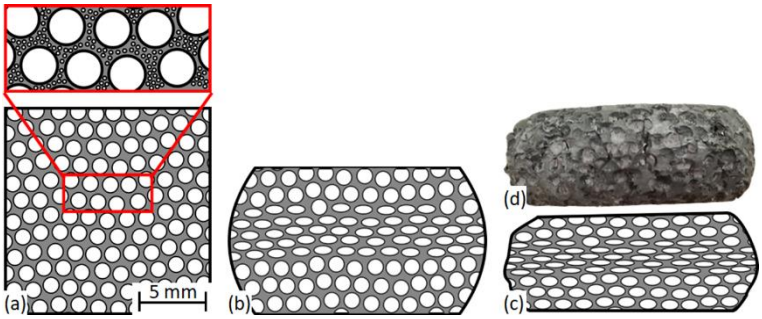

Figure 6. Failure mode of H/D=1 bimodal MMSFs: (a) initial state, (b) 25% deformation, (c) 50% deformation and (d) macro image of a sample.

The situation is changed in the case of higher aspect ratios (H/D=1.5 and 2.0), since in this case the probability of an inner defect is higher due to the larger volume and the volume is large enough for the appearance of one or more shear cracks. As it can be seen in fig. 7, at higher deformations a cleavage crack appeared in the samples (and correspondingly sharp stress peaks are plotted in the stress – strain graphs of figs. 4b and 4c), dividing the samples into two halves along a ~45° plane with respect to the vertical compressive force. With the appearance of this first cleavage like deformation zone a stress drop is recognized in the stress – strain curves. During the further deformation of the sample, the sample halves slid on each other until they reached the opposite compression plate resulting in further stress increment and in the appearance of a second cleavage crack in the samples. This was followed by further deformation of the sample halves. In the H/D=1.5 case there was no room for the complete evaluation of the second crack and the result was a 'V' like crack. In the case of H/D=2.0, the second crack could develop further similarly to the first one and an 'X' shape final crack was visible on the samples.

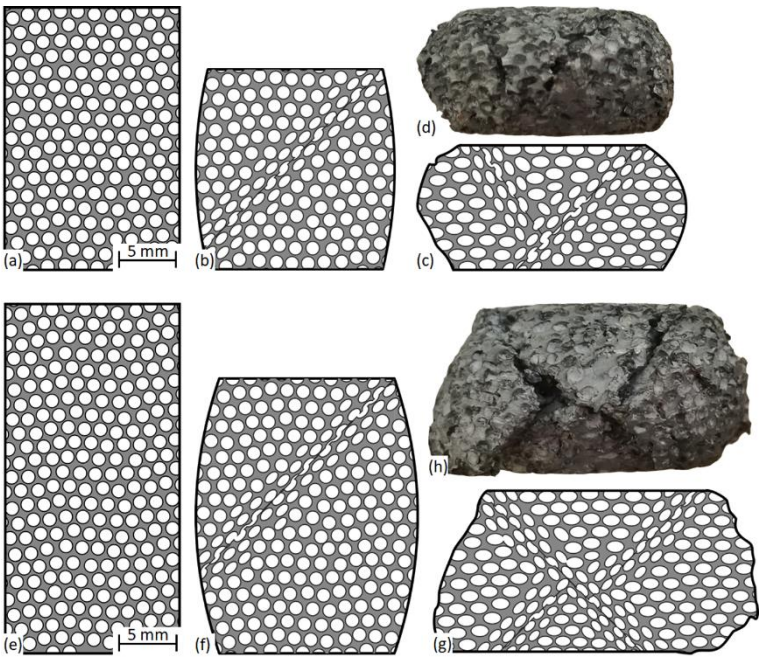

Figure 7. Failure mode of H/D=1.5 and H/D=2.0 bimodal MMSFs: (a and e) initial states, (b and f) 25% deformations, (c and g) 50% deformations and (d and h) macro images of a sample.

Due to the formation of sample halves in the case of higher aspect ratios, the energy absorption could not be complete, since large parts of the samples were not affected by the deformation. This

confirms further the need of constraint that helps to concentrate the deformation in the whole volume in order to have higher energy absorption.

4. Conclusions

In summary, this paper represents the basic microstructural and mechanical properties of AlSi12 matrix syntactic foams filled by small (~150 μm), large (~1500 μm) and mixed CHSs made of the mixture of alumina and silica. From the detailed investigations the following conclusions can be drawn.

- Pressure infiltration technique is applicable to produce bimodal MMSF structures. The infiltration investigated through macroscopic (CT) and microscopic (LOM, SEM) investigations proved sufficient infiltration.
- Over H/D=1, the engineering stress – strain curve if the samples showed a second local peak, connected to the appearance of a secondary cleavage crack during the failure.
- The mechanical properties of the bimodal samples laid between the pure small and pure large CHS filled MMSFs and the most important compressive strength can be reliably estimated by the rule of mixtures. This suggests that, the mechanical properties of the bimodal MMSFs can be tailored for the requirements of a given application by varying the ratio of the small and large CHSs.
- Because of their high compressive strength, the pure small CHS filled MMSFs can be suitable for structural applications.
- The bimodal and pure large CHS filled MMSFs can be suitable for energy absorption purposes, since the stress level of energy absorption is quite low and therefore the reaction forces in the case of a collision for instance would be lower. The energy absorption could be increased by longer damping routes and / or constrained deformation.

Acknowledgements

The research reported in this paper was supported by the Higher Education Excellence Program of the Ministry of Human Capacities in the frame of Nanotechnology research area of Budapest University of Technology and Economics (BME FIKP-NAT). The CT measurements were carried out as part of the GINOP-2.3.2-15-2016-00027 ‘Sustainable operation of the workshop of excellence for the research and development of crystalline and amorphous nanostructured materials’ project implemented in the framework of the Szechenyi 2020 program. The realization of this project is supported by the European Union.

Data availability

The raw/processed data required to reproduce these findings cannot be shared at this time as the data also forms part of an ongoing study.

References

[1] Orbulov IN. Compressive properties of aluminium matrix syntactic foams. Mater Sci Eng A 2012;555:52–6. doi:10.1016/j.msea.2012.06.032.

[2] Zou LC, Zhang Q, Pang BJ, Wu GH, Jiang LT, Su H. Dynamic compressive behavior of aluminum matrix syntactic foam and its multilayer structure. vol. 45. 2013. doi:10.1016/j.matdes.2012.08.015.

[3] Lin Y, Zhang Q, Ma X, Wu G. Mechanical behavior of pure Al and Al–Mg syntactic foam composites containing glass cenospheres. Compos Part A Appl Sci Manuf 2016;87:194–202. doi:10.1016/j.compositesa.2016.05.001.

[4] Mondal DP, Das S, Ramakrishnan N, Uday Bhasker K. Cenosphere filled aluminum syntactic foam made through stir-casting technique. Compos Part A Appl Sci Manuf 2009;40:279–88. doi:10.1016/j.compositesa.2008.12.006.

[5] Szlancsik A, Katona B, Májlinger K, Orbulov IN. Compressive behavior and microstructural characteristics of iron hollow sphere filled aluminum matrix syntactic foams. Materials (Basel) 2015;8:7926–37. doi:10.3390/ma8115432.

[6] Su MM, Wang H, Li KY, Hao H. Microstructure and Compressive Properties of Al/Al2O3 Syntactic Foams. Porous Met. Met. Foam., vol. 933, Trans Tech Publications; 2018, p. 174–81. doi:10.4028/www.scientific.net/MSF.933.174.

[7] Vogiatzis CA, Tsouknidas A, Kountouras DT, Skolianos SM. Aluminum–ceramic cenospheres syntactic foams produced by powder metallurgy route. Mater Des 2015;85:444–54. doi:10.1016/j.matdes.2015.06.154.

[8] Licitra L, Luong DD, Strbik OM, Gupta N. Dynamic properties of alumina hollow particle filled aluminum alloy A356 matrix syntactic foams. Mater Des 2015;66:504–15. doi:10.1016/j.matdes.2014.03.041.

[9] Balch DK, O'Dwyer JG, Davis GR, Cady CM, Gray GT, Dunand DC. Plasticity and damage in aluminum syntactic foams deformed under dynamic and quasi-static conditions. Mater Sci Eng A 2005;391:408–17. doi:10.1016/j.msea.2004.09.012.

[10] Vogiatzis CA, Skolianos SM. On the sintering mechanisms and microstructure of aluminium–ceramic cenospheres syntactic foams produced by powder metallurgy route. Compos Part A Appl Sci Manuf 2016;82:8–19. doi:10.1016/j.compositesa.2015.11.037.

[11] Myers K, Katona B, Cortes P, Orbulov IN. Quasi-static and high strain rate response of aluminum matrix syntactic foams under compression. Compos Part A Appl Sci Manuf 2015;79:82–91. doi:10.1016/j.compositesa.2015.09.018.

[12] Rohatgi PK, Kim JK, Gupta N, Alaraj S, Daoud A. Compressive characteristics of A356/fly ash cenosphere composites synthesized by pressure infiltration technique. Compos Part A Appl Sci Manuf 2006;37:430–7. doi:10.1016/j.compositesa.2005.05.047.

[13] Anbuchezhiyan G, Muthuramalingam T, Mohan B. Effect of process parameters on mechanical properties of hollow glass microsphere reinforced magnesium alloy syntactic foams under vacuum die casting. Arch Civ Mech Eng 2018;18:1645–50. doi:10.1016/J.ACME.2018.07.008.

[14] Anantharaman H, Shunmugasamy VC, Strbik OM, Gupta N, Cho K. Dynamic properties of silicon carbide hollow particle filled magnesium alloy (AZ91D) matrix syntactic foams. Int J Impact Eng 2015;82:14–24. doi:10.1016/j.ijimpeng.2015.04.008.

[15] Nguyen QB, Sharon Nai ML, Nguyen AS, Seetharaman S, Wai Leong EW, Gupta M. Synthesis and properties of light weight magnesium-cenosphere composite. Mater Sci Technol (United

Kingdom) 2016;32:923–9. doi:10.1080/02670836.2015.1104017.

[16] Rohatgi PK, Daoud A, Schultz BF, Puri T. Microstructure and mechanical behavior of die casting AZ91D-Fly ash cenosphere composites. Compos Part A Appl Sci Manuf 2009;40:883–96. doi:10.1016/j.compositesa.2009.04.014.

[17] Peroni L, Scapin M, Avalle M, Weise J, Lehmhus D. Dynamic mechanical behavior of syntactic iron foams with glass microspheres. Mater Sci Eng A 2012;552:364–75. doi:10.1016/j.msea.2012.05.053.

[18] Luong DD, Shunmugasamy VC, Gupta N, Weise J, Baumeister J. Quasi-static and high strain rates compressive response of iron and Invar matrix syntactic foams. Mater Des 2015;66:516–31. doi:10.1016/j.matdes.2014.07.030.

[19] Peroni L, Scapin M, Avalle M, Weise J, Lehmhus D, Baumeister J, et al. Syntactic Iron Foams - On Deformation Mechanisms and Strain-Rate Dependence of Compressive Properties. Adv Eng Mater 2012;14:909–18. doi:10.1002/adem.201200160.

[20] Mondal DP, Datta Majumder J, Jha N, Badkul A, Das S, Patel A, et al. Titanium-cenosphere syntactic foam made through powder metallurgy route. Mater Des 2012;34:82–9. doi:10.1016/j.matdes.2011.07.055.

[21] Mandal DP, Majumdar DD, Bharti RK, Majumdar JD. Microstructural characterisation and property evaluation of titanium cenosphere syntactic foam developed by powder metallurgy route. Powder Metall 2015;58:289–99. doi:10.1179/1743290115Y.0000000012.

[22] Jha N, Mondal DP, Goel MD, Majumdar JD, Das S, Modi OP. Titanium cenosphere syntactic foam with coarser cenosphere fabricated by powder metallurgy at lower compaction load. Trans Nonferrous Met Soc China 2014;24:89–99. doi:10.1016/S1003-6326(14)63032-6.

[23] Movahedi N, Murch EG, Belova VI, Fiedler T. Effect of Heat Treatment on the Compressive Behavior of Zinc Alloy ZA27 Syntactic Foam. Materials (Basel) 2019;12. doi:10.3390/ma12050792.

[24] Linul E, Lell D, Movahedi N, Codrean C, Fiedler T. Compressive properties of zinc syntactic foams at elevated temperatures. Compos Part B Eng 2018. doi:10.1016/J.COMPOSITESB.2018.12.019.

[25] Pan L, Yang Y, Ahsan MU, Luong DD, Gupta N, Kumar A, et al. Zn-Matrix Syntactic Foams: Effect of Heat Treatment on Microstructure and Compressive Properties. Mater Sci Eng A 2018;731:413–22. doi:10.1016/j.msea.2018.06.072.

[26] Daoud A. Effect of strain rate on compressive properties of novel Zn12Al based composite foams containing hybrid pores. Mater Sci Eng A 2009;525:7–17. doi:10.1016/j.msea.2009.05.038.

[27] Sánchez-Martínez A, Cruz A, González-Nava M, Suárez MA. Main process parameters for manufacturing open-cell Zn-22Al-2Cu foams by the centrifugal infiltration route and mechanical properties. Mater Des 2016;108:494–500. doi:10.1016/j.matdes.2016.07.032.

[28] Manoj, Afzal Khan DM, Mondal DP. High temperature deformation behavior of closed cell ZnAl27 hybrid foam made through stir casting technique. Mater Sci Eng A 2018;731:324–30. doi:10.1016/j.msea.2018.06.044.

[29] Luong DD, Gupta N, Daoud A, Rohatgi PK. High strain rate compressive characterization of aluminum alloy/fly ash cenosphere composites. JOM 2011;63:53–6. doi:10.1007/s11837-011-0029-y.

[30] Huang Z, Yu S, Liu J, Zhu X. Microstructure and mechanical properties of in situ Mg2Si/AZ91D composites through incorporating fly ash cenospheres. Mater Des 2011;32:4714–9. doi:10.1016/j.matdes.2011.06.043.

[31] Luong DD, Gupta N, Rohatgi PK. The high strain rate compressive response of Mg-Al alloy/fly Ash cenosphere composites. JOM 2011;63:48–52. doi:10.1007/s11837-011-0028-z.

[32] Ramachandra M, Radhakrishna K. Synthesis-microstructure-mechanical properties-wear and corrosion behavior of an Al-Si (12{%})---Flyash metal matrix composite. J Mater Sci 2005;40:5989–97. doi:10.1007/s10853-005-1303-6.

[33] Santa Maria JA, Schultz BF, Ferguson JB, Rohatgi PK. Al–Al2O3 syntactic foams – Part I: Effect of matrix strength and hollow sphere size on the quasi-static properties of Al-A206/Al2O3 syntactic foams. Mater Sci Eng A 2013;582:415–22. doi:10.1016/j.msea.2013.05.081.

[34] Ferguson JB, Santa Maria JA, Schultz BF, Rohatgi PK. Al–Al2O3 syntactic foams—Part II: Predicting mechanical properties of metal matrix syntactic foams reinforced with ceramic spheres. Mater Sci Eng A 2013;582:423–32. doi:10.1016/j.msea.2013.06.065.

[35] Omar MY, Xiang C, Gupta N, Strbik OM, Cho K. Syntactic foam core metal matrix sandwich composite under bending conditions. Mater Des 2015;86:536–44. doi:10.1016/j.matdes.2015.07.127.

[36] Santa Maria JA, Schultz BF, Ferguson JB, Gupta N, Rohatgi PK. Effect of hollow sphere size and size distribution on the quasi-static and high strain rate compressive properties of Al-A380--Al2O3 syntactic foams. J Mater Sci 2014;49:1267–78. doi:10.1007/s10853-013-7810-y.

[37] Luong DD, Strbik OM, Hammond VH, Gupta N, Cho K. Development of high performance lightweight aluminum alloy/SiC hollow sphere syntactic foams and compressive characterization at quasi-static and high strain rates. J Alloys Compd 2013;550:412–22. doi:10.1016/j.jallcom.2012.10.171.

[38] Cox J, Luong DD, Shunmugasamy VC, Gupta N, Strbik OM, Cho K. Dynamic and Thermal Properties of Aluminum Alloy A356/Silicon Carbide Hollow Particle Syntactic Foams. Metals (Basel) 2014;4:530–48. doi:10.3390/met4040530.

[39] Vendra LJ, Neville B, Rabiei A. Fatigue in aluminum–steel and steel–steel composite foams. Mater Sci Eng A 2009;517:146–53. doi:10.1016/j.msea.2009.03.075.

[40] Castro G, Nutt SR. Synthesis of syntactic steel foam using gravity-fed infiltration. Mater Sci Eng A 2012;553:89–95. doi:10.1016/j.msea.2012.05.097.

[41] Vendra LJ, Rabiei A. A study on aluminum–steel composite metal foam processed by casting. Mater Sci Eng A 2007;465:59–67. doi:10.1016/j.msea.2007.04.037.

[42] Taherishargh M, Belova IV, Murch GE, Fiedler T. Low-density expanded perlite–aluminium syntactic foam. Mater Sci Eng A 2014;604:127–34. doi:10.1016/j.msea.2014.03.003.

[43] Taherishargh M, Sulong MA, Belova IV, Murch GE, Fiedler T. On the particle size effect in expanded perlite aluminium syntactic foam. Mater Des 2015;66:294–303. doi:10.1016/j.matdes.2014.10.073.

[44] Taherishargh M, Linul E, Broxtermann S, Fiedler T. The mechanical properties of expanded perlite-aluminium syntactic foam at elevated temperatures. J Alloys Compd 2018;737:590–6. doi:10.1016/J.JALLCOM.2017.12.083.

[45] Broxtermann S, Taherishargh M, Belova IV, Murch GE, Fiedler T. On the compressive behaviour of high porosity expanded Perlite-Metal Syntactic Foam (P-MSF). J Alloys Compd

2017;691:690–7. doi:10.1016/j.jallcom.2016.08.284.

[46] Taherishargh M, Belova IV, Murch GE, Fiedler T. The effect of particle shape on mechanical properties of perlite/metal syntactic foam. J Alloys Compd 2017;693:55–60. doi:10.1016/j.jallcom.2016.09.168.

[47] Borovinšek M, Taherishargh M, Vesenjak M, Ren Z, Fiedler T. Geometrical characterization of perlite-metal syntactic foam. Mater Charact 2016;119:209–15. doi:10.1016/j.matchar.2016.07.024.

[48] Fiedler T, Taherishargh M, Krstulović-Opara L, Vesenjak M. Dynamic compressive loading of expanded perlite/aluminum syntactic foam. Mater Sci Eng A 2015;626:296–304. doi:10.1016/j.msea.2014.12.032.

[49] Taherishargh M, Belova IV, Murch GE, Fiedler T. On the mechanical properties of heat-treated expanded perlite–aluminium syntactic foam. Mater Des 2014;63:375–83. doi:10.1016/j.matdes.2014.06.019.

[50] Taherishargh M, Belova IV, Murch GE, Fiedler T. Pumice/aluminium syntactic foam. Mater Sci Eng A 2015;635:102–8. doi:10.1016/j.msea.2015.03.061.

[51] Májlinger K. Wear properties of hybrid AlSi12 matrix syntactic foams. Int J Mater Res 2015;106:1165–73. doi:10.3139/146.111290.

[52] Orbulov IN, Májlinger K. Characterisation of hybrid metal matrix syntactic foams. Mater Sci Forum 2015;812:219–25. doi:10.4028/www.scientific.net/MSF.812.219.

[53] Májlinger K, Bozóki B, Kalácska G, Keresztes R, Zsidai L. Tribological properties of hybrid aluminum matrix syntactic foams. Tribol Int 2016;99:211–23. doi:10.1016/j.triboint.2016.03.032.

[54] Májlinger K, Orbulov IN. Characteristic compressive properties of hybrid metal matrix syntactic foams. Mater Sci Eng A 2014;606:248–56. doi:10.1016/j.msea.2014.03.100.

[55] Tao XF, Zhang LP, Zhao YY. Al matrix syntactic foam fabricated with bimodal ceramic microspheres. vol. 30. 2009. doi:10.1016/j.matdes.2008.11.005.

[56] Brouwers HJH. Particle-size distribution and packing fraction of geometric random packings. Phys Rev E 2006;74:31309. doi:10.1103/PhysRevE.74.031309.

[57] ISO13314:2011 Mechanical testing of metals - Ductility testing - Compression test for porous and cellular metals 2011.

[58] Lachambre J, Maire E, Adrien J, Choqueuse D. In situ observation of syntactic foams under hydrostatic pressure using X-ray tomography. Acta Mater 2013;61:4035–43. doi:10.1016/j.actamat.2013.03.017.

[59] Adrien J, Maire E, Gimenez N, Sauvant-Moynot V. Experimental study of the compression behaviour of syntactic foams by in situ X-ray tomography. Acta Mater 2007;55:1667–79. doi:10.1016/j.actamat.2006.10.027.

[60] Mankovits T, Varga TA, Manó S, Kocsis I. Compressive Response Determination of Closed-Cell Aluminium Foam and Linear-Elastic Finite Element Simulation of μCT-Based Directly Reconstructed Geometrical Models. Strojniški Vestn - J Mech Eng Vol 64, No 2 Strojniški Vestn - J Mech Eng 2018. doi:10.5545/sv-jme.2017.5048.

[61] Mankovits T, Budai I, Balogh G, Gábora A, Kozma I, Varga T, et al. Structural analysis and its statistical evaluation of a closed-cell metal foam. Int Rev Appl Sci Eng 2014;5:135–43.

doi:10.1556/IRASE.5.2014.2.5.

[62] Orbulov IN, Dobránszky J, Németh Á. Microstructural characterisation of syntactic foams. J Mater Sci 2009;44:4013–9. doi:10.1007/s10853-009-3552-2.

[63] Kádár C, Máthis K, Orbulov IN, Chmelík F. Monitoring the failure mechanisms in metal matrix syntactic foams during compression by acoustic emission. vol. 173. 2016. doi:10.1016/j.matlet.2016.02.102.

[64] Szlancsik A, Katona B, Dombóvári Z, Orbulov IN. On the effective Young's modulus of metal matrix syntactic foams. Mater Sci Technol 2017;33:2283–9. doi:10.1080/02670836.2017.1374497.

[65] Chernousov AA, Chan BYB. Optimising in-situ nitridation in piled aluminium flakes for novel closed cell composites with high fracture stress and toughness. Mater Des 2018;150:113–23. doi:10.1016/j.matdes.2018.04.020.

[66] Orbulov IN, Ginsztler J. Compressive characteristics of metal matrix syntactic foams. Compos Part A Appl Sci Manuf 2012;43:553–61. doi:10.1016/j.compositesa.2012.01.008.

[67] Orbulov IN, Májlinger K. Compressive Properties of Metal Matrix Syntactic Foams in Free and Constrained Compression. JOM 2014;66:882–91. doi:10.1007/s11837-014-0914-2.